**ICESat-2 and ocean particulates: Building a roadmap for calculating $K_d$ from space-based lidar photon profiles**

Eidam, E.F.[1+], Bisson, K.[2], Wang, C.[3], Walker, C.[4], Gibbons, A.[5]

[1] Oregon State University, College of Earth, Ocean, and Atmospheric Sciences. Corvallis, OR, USA.
[2] NASA Ocean Biology & Biogeochemistry Program, NASA Headquarters, Washington, D.C., USA
[3] University of North Carolina at Chapel Hill, Department of Earth, Marine, and Environmental Sciences, Chapel Hill, NC, USA
[4] Woods Hole Oceanographic Institute, Woods Hole, MA, USA
[5] NASA Goddard Space Flight Center, Greenbelt, MD, USA



## Abstract

ICESat-2's Advanced Topographic Laser Altimeter System (ATLAS) has emerged as useful tool for calculating attenuation signals in natural surface waters, thus improving our understanding of particulates from open-ocean plankton to nearshore suspended terrigenous sediments. While several studies have employed methods based on Beer's Law to derive attenuation coefficients (including through a machine-learning approach), a rigorous sensitivity test on specific tuning parameters and processing choices has not yet been performed. Here we present comprehensive sensitivity tests of solar background removal, noise removal, choice of bin sizes, surface-peak exclusion, and beam pairing across four contrasting marine environments as well as two contrasting daytime/nighttime examples to quantify the impact of these processing choices on the derived photon-based attenuation coefficient $K_{dph}$. Horizontal and vertical bin sizes caused 6-13% variation in results, and adjusting the starting depth for calculations (i.e., the exclusion depth for the noisy sea-surface peak) caused 17% variation in results. Pairing data from strong and weak beams caused ~6-11% variation in results. In some environments, daytime data could be reasonably salvaged, but in others the results were not reliable. Detailed information about processing choices and a suggested workflow for ocean applications are provided. The sensitivity test results and suggested workflow pave the way for expanded $K_{dph}$ analyses of global datasets (including turbid coastal waters) as well as interdisciplinary applications, such as evaluating nearshore ecological processes related to sediment dynamics and light attenuation.

## Highlights

1. Uncover subsurface attenuation insights from ICESat-2 ATL03.
2. Identified key factors influencing attenuation calculations.
3. Established robust best practices for deriving $K_{dph}$

+ *Author contact: Dr. Emily Eidam, emily.eidam@oregonstate.edu*

## 1. Introduction

Ocean optics is the primary link between ocean biology and observations made from satellites in space (Siegel et al., 2005; Jamet et al., 2019). Both particulate materials (e.g., phytoplankton, zooplankton, detritus) and dissolved materials (e.g., colored dissolved material) in the water column play a role in this relationship (Collister et al., 2018). They affect the light field by absorbing and scattering downwelling light. The effects of these processes can be expressed through a single parameter describing the decay of light with depth, $K_d$ (diffuse attenuation coefficient, $m^{-1}$). $K_d$ is a quasi inherent optical property because it also depends on the apparent light environment. Values of $K_d$ from traditional ocean color methods have been used for a variety of science applications, including measurements of turbidity (e.g., Doxaran et al., 2002; Acker et al., 2005; Barnes et al., 2015) and phytoplankton chlorophyll (Morel, 1988, Morel and Maritorena, 2001, Lee et al., 2002). One major limitation of ocean color is the requirement of sunlit waters, whereas active sensors (lidar) can operate in darkness, thus generating far more data than are available from traditional methods alone. Although no dedicated ocean lidar currently exists, orbiting lidar satellites have offered a wealth of information about the ocean subsurface at all times of the year, including discoveries of zooplankton diel vertical migration from space (Behrenfeld et al. 2019), seasonal biases in ocean color products (Bisson et al. 2021a), phytoplankton blooms at the sea ice edge (Lu et al., 2020, Horvat et al. 2022, Bisson and Cael, 2021) and polar phytoplankton annual cycles (Behrenfeld et al. 2017).

The Ice, Cloud, and land Elevation Satellite-2 (ICESat-2) is the most powerful lidar altimeter currently in orbit (Markus et al. 2017), and since its launch in 2018, a growing number of studies have derived $K_d$ in order to address science questions or compare performance with traditional ocean color (Lu et al. 2020, 2021a, Corcoran and Parrish, 2021, Yang et al. 2023, Zhang et al. 2022). Another lidar satellite recently in orbit that was used for ocean studies, the Cloud-Aerosol Lidar and Infrared Pathfinder Satellite Observations (CALIPSO) satellite, carried the Cloud-Aerosol Lidar with Orthogonal Polarization (CALIOP) instrument. ICESat-2 attenuation products must be generated by the user from low-level photon data (i.e., from ATL03 photon point clouds), while that of CALIPSO is already quality controlled, validated, and freely available online (Bisson et al, 2021b, Behrenfeld et al. 2022). As such, a number of approaches to generate $K_{dph}$ have been proposed, and these approaches range in complexity, computational requirements, and user knowledge. The potential of ICESat-2 data to transform our understanding of subsurface ocean activity is hindered by a lack of understanding of the true uncertainties involved in deriving these products. Currently it is not clear how environmental conditions (wave height, bubbles) and/or engineering limitations (signal strength, signal-to-noise) affect downstream values of $K_{dph}$, or how sensitive estimates of $K_{dph}$ are to subjective user preferences of horizontal or vertical bin size. As more observations are added to the record and there is an increasing interest in using this data for (subsurface) oceanographic applications, it has become increasingly important to define which processing steps are essential for deriving quality $K_{dph}$ measurements from ICESat-2 observations, and which ones are unnecessary.

In the simplest example, one can download photon cloud data from a single beam in the ATL03 geolocated photon product, assemble the geotagged subsurface photons into vertical bins, and calculate the decay exponent as $K_d$ using Beer's Law (Lu et al. 2020, 2021a, Zheng et al. 2022). In a far more computationally costly case, one could download ATL03 data, assemble photons from different beams together into a single photon cloud, remove the solar background photon count, remove segments in the along-track direction that exhibit saturated signals (and other quality control checks), deconvolute the signal to remove after pulses using an estimate of the system's impulse response function (Lu et al. 2020), apply one of several methods for removing the surface peak (i.e., to salvage as much near-surface data as possible), and calculate the attenuation coefficient. In an intermediate case, minimal signal quality control is required with an ensemble machine-learning approach (Corcoran and Parrish, 2020), which avoids additional preprocessing procedures and user expertise as the algorithms learn data associations, even in the presence of noise. With this variety of methods, it is important to determine if $K_{dph}$ calculated from different methods results in a substantially different answer. Furthermore, it is essential to understand the sensitivity of these derived $K_{dph}$ values to different processing considerations. ICESat-2 ATL03 data are large (450 GB per day) and even when land data are excluded, it is advisable to reduce computational requirements and streamline processing when possible, especially for future assessments of $K_{dph}$ values across regional to global scales.

Our study is thus motivated by the following questions:

- What environmental and engineering factors govern whether or not a photon cloud is suitable to extract subsurface information?
- How much processing is needed to extract meaningful $K_{dph}$ values, and which processing steps are most influential to the values obtained?

Here we provide case studies and sensitivity tests to illustrate a range of environmental and subjective (processing choice) barriers for achieving computationally consistent subsurface properties from ICESat-2 data. Our goal is to inform future work that may ultimately use a batch processing routine to process ICESat-2 data more efficiently and on global scales. We envision future scientific applications of ICESat-2 data that are supported by well-defined methodological uncertainties, in order to enhance the capabilities of ICESat-2 for answering ocean questions.

## 2. Data sources and case study selection

### *2.1 ICESat-2 ATL03 product*

The Advanced Topographic Laser Altimeter System (ATLAS) is the primary instrument onboard ICESat-2, and contains a 532 nm laser with a pulse repetition rate of 10 kHz which generates three pairs of beams (three strong beams and three weak beams). The spot size on the ground for each beam is 11 m (Magruder et al. 2020). ICESat-2 has a 91-day revisit cycle with higher sampling density at the poles. Level-2 geolocated photon cloud data, derived from raw photon times-of-flight and corrected telemetry, are cataloged in the ATL03 product, version 6 (Neumann et al., 2021, [https://nsidc.org/data/atl03/versions/6](https://nsidc.org/data/atl03/versions/6)). In this work, these have been downloaded using icepyx

(Scheick et al. 2019) or directly through OpenAltimetry, which is hosted by the NASA EarthData portal (www.earthdata.nasa.gov/technology/openaltimetry). The primary variables used in analyses are photon ellipsoidal height (meters) and relative along-track distance (meters) derived from the individual photon geolocations. Additional quality-control and metadata variables of interest are itemized in the Methods and Table 1.

### *2.2 Case study site selection for sensitivity analyses*

In this study, our primary goal is to explore and test different strategies for processing ATL03 photon clouds in near-surface waters of the coastal and open ocean. We chose to analyze data from two sites that represent end member conditions in the ocean (in terms of chlorophyll concentration and particle load), and two sites where contrasting day and night returns were gathered (in order to allow for solar background sensitivity tests). One of the day/night sites also exhibited common issues of afterpulse and impulse response noise. We performed sensitivity tests on different processing steps for these sites with the goal of assessing variation in derived $K_{dph}$ products.

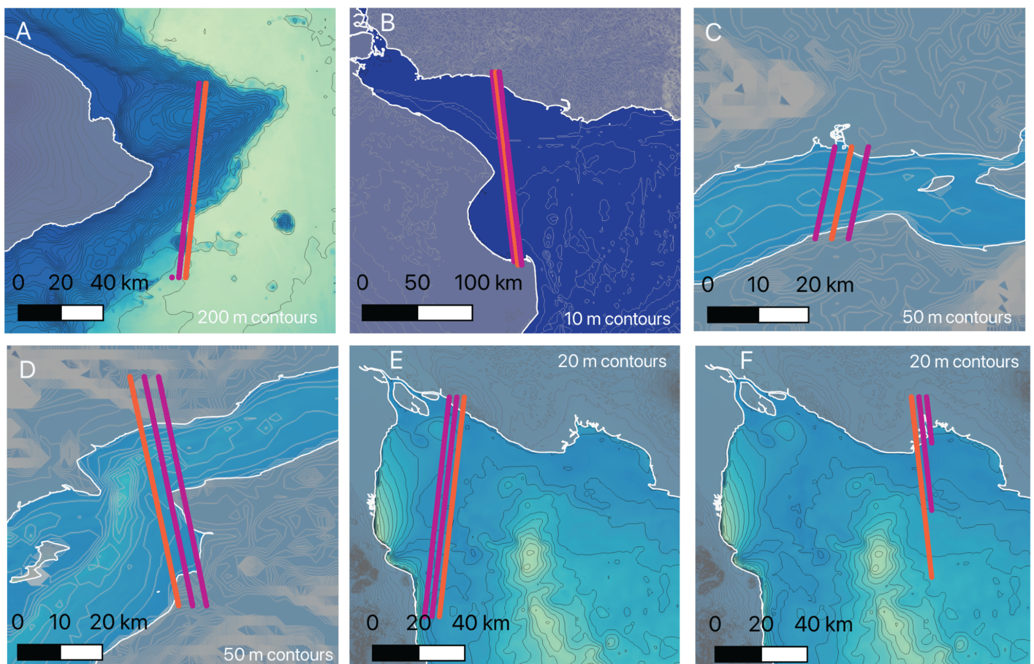


**Figure 1**. Map of sites chosen for analyses. A) Track 0472, east side of Hawai'i. B) Track 1039, Rio de la Plata. C) Track 0594, upper Cook Inlet, Alaska. D) Track 0632, middle Cook Inlet, Alaska. E) Track 1141, Colorado River Delta / upper Baja California. F) Track 0341, upper Baja California. See Table 1 for additional details and measurement dates. Orange lines denote the beam (or beam pair) that was used for analyses.

The first site was located east of the island of Lanai in Hawaii (Figs. 1A, 2A) and was selected to be adjacent to long-term monitoring station MOBY (Marine Optical BuoY), an ocean-color validation site for remote sensing products where monthly cruises collect radiometry data. It is expected that in the future, these in situ data may be useful for $K_{dph}$ validation. Using in situ measurements for validation is preferred over ocean color data from passive satellite sensors which is known to have various errors (Bisson et al. 2021a,b) and offers a less rigorous comparison to derived ICESat-2 attenuation coefficients. The MOBY site represents an open ocean (oligotrophic) location with low biomass and low sediment input (i.e., low $K_{dph}$), where wave activity and white caps may introduce more pronounced environmental challenges into the low signal. The first optical depth in Hawaiian waters is typically greater than 100 m. We chose this site to introduce a case where the derived $K_{dph}$ may be near the signal detection limit of ICESat-2.

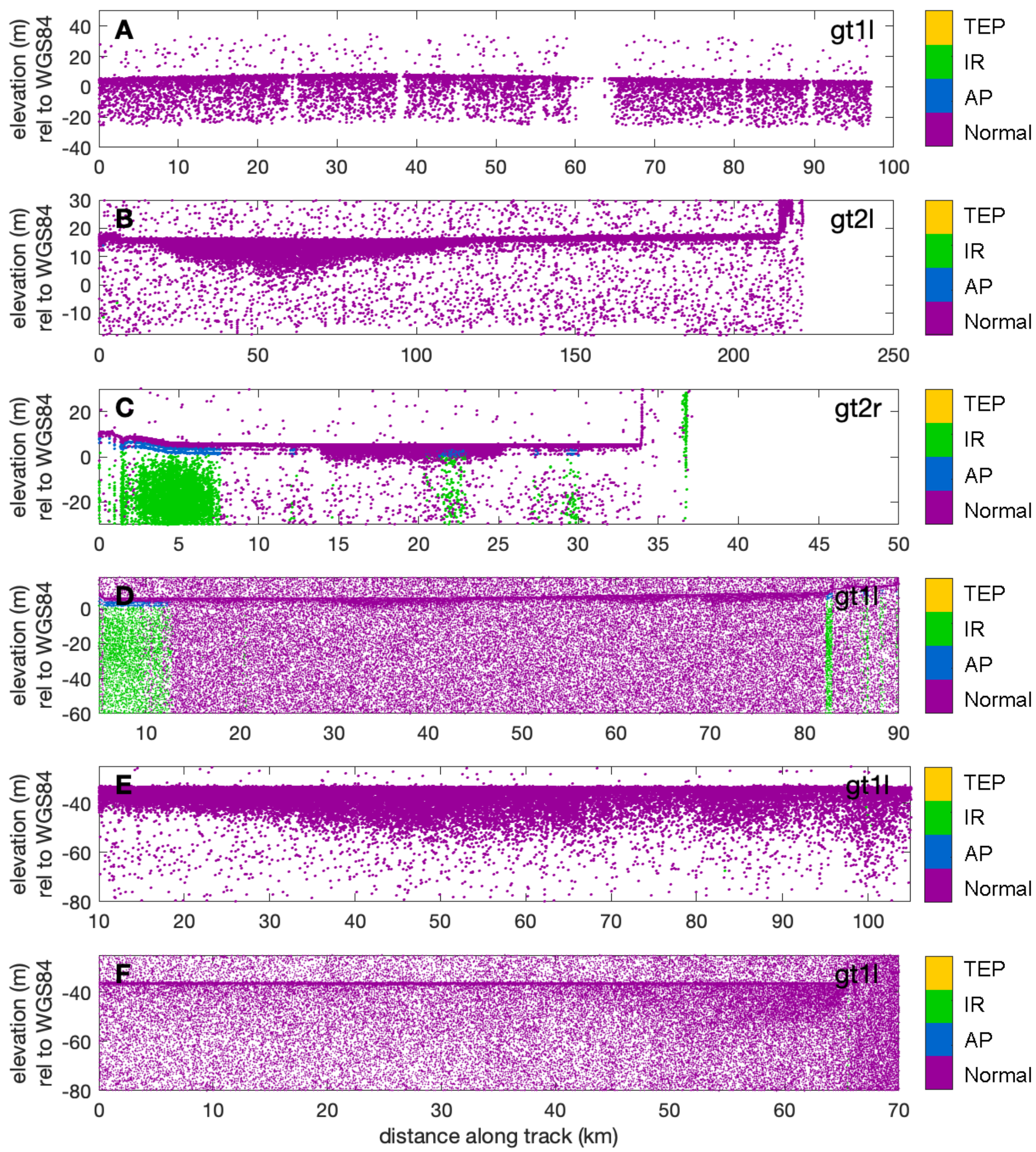


**Figure 2**. Photon clouds for selected lines. A) Track 0472, east side of Hawai'i. B) Track 1039, Rio de la Plata. C) Track 0594, Cook Inlet, Alaska. D) Track 0067, Columbia River mouth. See Table 1 for additional details and measurement dates. Photons are classified according to the *quality_ph* flag as detailed in Table 2. Photon data from one of six tracks is presented in each subplot; the track is noted in the upper right (e.g., gt2l = ground track 2 left). In all cases data from a strong beam are plotted.

Next we acquired data from Rio de la Plata (Figs. 1B, 2B), a coastal estuary in Argentina where suspended-sediment loads are often high. The entrance to the estuary is wide, meaning several tens of kilometers of ATL03 data can be downloaded which span strong gradients in suspended-sediment concentrations, and thus allow for analysis of variability in derived $K_{dph}$.

For day versus night analyses and afterpulse analyses, we included two selections of data from Cook Inlet (Figs. 1C, D; 2C, D) which illustrate some of the common problems seen in ATL03 ocean data. Much like Rio de la Plata, Cook Inlet exhibits high suspended-sediment loads and strong cross-bay gradients (related to strong tidal action). The first section (Fig. 2C) is from nighttime and exhibits impulse response and afterpulsing (discussed in section 3.3). This section is used as a case study to determine whether noisy data are salvageable for evaluation of $K_{dph}$. The second section (Fig. 2D) is from daytime and is used to evaluate the impact of the solar background on attenuation values. The final site was upper Baja California near the Colorado River Delta. This site was chosen in order to explore day versus night returns, but in an environment with lower turbidity than Cook inlet.

Details of each site including general water properties, bathymetry, solar elevation (indicating daytime versus nighttime signals), and solar background rate are provided in Table 1.

**Table 1**. Details of sites, tracklines, and dates chosen for analyses (maps are presented in Fig. 1).

| **Track** | **Date** | **Site** | **Bathy** | **General optical properties** | **Mean solar elevation (deg above E-N plane)** | **Mean solar background rate* (photons/m$^{-1}$) and [reference elevation] (m)** |
|---|---|---|---|---|---|---|
| 0472 (Fig. 2A) | 2022-01-22 | East side of Hawaiian islands, USA | Deep (>1000 m) | Generally optically clear | -11 | 0.11 [11 to 31] |
| 1039 (Fig. 2B) | 2022-05-30 | Rio de la Plata, Argentina/ Uruguay border | Shallow (<20 m) | Generally turbid due to fluvial input and estuarine circulation | -75 | 0.26 [19 to 41] |
| 0594 (Fig. 2C) | 2021-08-01 | Cook Inlet, southcentral Alaska, USA | Moderately shallow (<50 m) | Generally turbid due to glacial-fluvial input and strong tidal action | -3.6 | 0.11 [29 to 228] |
| 0632 (Fig. 2D) | 2020-08-05 | Cook Inlet, southcentral Alaska, USA | Moderately shallow (<50 m) | Generally turbid due to glacial-fluvial input and strong tidal action | 26 | 8.5 [18 to 242] |
| 1141 (Fig. 2E) | 2023-03-05 | Colorado River Delta / upper Baja California | Moderately shallow (<100 m) | Low to moderate turbidity depending on river flow | -61 | 0.07 [-25 to 12] |
| 0341 (Fig. 2F) | 2023-04-12 | Upper Baja California | Moderately shallow (<100 m) | Low to moderate turbidity depending on river flow | 44 | 8.8 [-33 to -14] |

** Rate is for the corresponding strong beams shown in Fig. 2 subsampled at 1-km horizontal intervals. Reference elevations are the heights relative to the WGS84 ellipsoid over which the number of photons was averaged.*

## 3.0 Methods

The first step in analyzing ATL03 photon data for ocean subsurface $K_{dph}$ values is to download data. This can be done (1) directly through openaltimetry.org accessed using a free account; (2) through python toolboxes like icepyx (https://icepyx.readthedocs.io/en/latest/index.html#) or SlideRule Earth (https://github.com/ICESat2-SlideRule), which allow users to work with data in the cloud; or (3) directly through the National Snow and Ice Data Center (NSIDC) website (https://nsidc.org/data/icesat-2) where ICESat-2 ATL data are hosted. Files are provided in a Hierarchical Data Format (commonly noted as hdf, or h5), which can be read using a coding package like HDF5 provided by www.hdfgroup.org. The ATL03 dataset contains a complex data structure which is described in the ATLAS data dictionary available through NSIDC (see Table 2). A brief summary of variables which are relevant to $K_{dph}$ processing are given in Table 2. The "Data structure location" field references the data structure group where variables can be found.

ATL03 data variables are characterized by diverse data dimensions. Raw photon XYZ data have varying dimensions based on the number of photons recorded per laser pulse and based on beam strength (the strong beam generally produces more photon returns), whereas other variables like solar elevation are reported at fixed, lower spatial resolutions (e.g., every 20 m along-track).

**Table 2**. Relevant variables for $K_d$ processing from ATL03 data (source: ATL03 Data Dictionary, https://nsidc.org/data/icesat-2/documents)

| **Variable** | **Data structure location** | **Notes about dimension / spatial resolution** | **Explanation** |
|---|---|---|---|
| quality_ph | /gtx/heights | Comparable to # of photons returned | Values:<br>0 - Nominal (normal)<br>1 - Possible afterpulse<br>2 - Possible impulse response<br>3 - Possible TEP |
| lon_ph | /gtx/heights | Comparable to # of photons returned | photon "x" (latitude) |
| lat_ph | /gtx/heights | Comparable to # of photons returned | photon "y" (latitude) |
| h_ph | /gtx/heights | Comparable to # of photons returned | photon "z" (height above WGS84 ellipsoid) |
| dist_ph_along | /gtx/heights | Comparable to # of photons returned | Photon distance along-track (projected to ellipsoid and relative to last equatorial crossing) (m) |
| solar_elevation | /gtx/geolocation | One value per 20-m segment | Elevation of sun above E-W plane relative to photon location (positive upward) (units of degrees) |
| near_sat_frac | /gtx/geolocation | One value per 20-m segment | Fraction of pulses within segment which are nearly saturated |
| full_sat_frac | /gtx/geolocation | One value per 20-m segment | Fraction of pulses within segment which are fully saturated |

After downloading the data, general steps for $K_{dph}$ analysis include:

(1) Excluding land data
(2) Determining if sufficient subsurface photons are present to warrant further analysis
(3) Removing noise (solar background and afterpulses, and impulse response if waters are very clear)
(4) Horizontal and vertical binning of the data to create histograms
(5) Using the maximum value in the histogram (where appropriate) to identify and removing the surface peak
(6) Correcting z coordinates for water refraction and re-calculating the histograms
(7) Applying other corrections as desired or as suitable (including aggregation of data from strong/weak beam pairs, seabed removal, etc.)
(8) Fitting of an exponential decay function to the cleaned histograms (Beer's Law)
(9) Evaluating results of results

Here we provide a detailed description of each suggested analysis step, including sensitivity tests for items (3), (4), (5), and (7).

### *3.1 Excluding land data*

While a land classification variable is available in ATL, it does not offer updated and fine-scale resolution in coastal regions. This limitation is problematic because $K_{dph}$ is often of interest in coastal regions near shorelines. To address this issue, a high-resolution land mask from an external source can be applied both to reduce processing times (by omitting unnecessary data) and to eliminate land pixels from $K_{dph}$ calculations. Here we suggest using the recently released 30-m global shoreline developed by Sayre et al. (2019) and provided by the USGS (https://rmgsc.cr.usgs.gov/gie/). Processing steps are outlined in Wang et al. (2023) and including extracting the USGS global vector

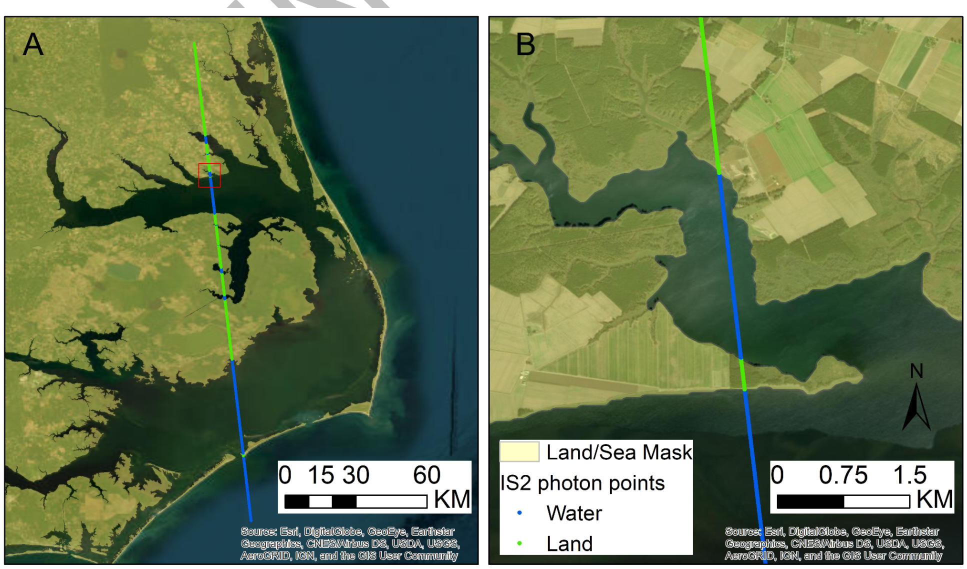


**Figure 3**. Illustration of ICESat-2 ATL03 photon data over NC coastal areas, with land and sea photons identified based on the land and sea mask dataset derived from the USGS global vector shoreline dataset.

shoreline datasets from Geodatabase (see Sayre et al., 2019) and converting it into a geopackage format, which is indexed for rapid spatial operations. To further enhance computational speed, we partition the global shoreline vector data into smaller geometric sections, each spanning 1-degree, to keep the spatial query load of the geometry small. This dataset may require periodic manual updates to keep pace with ever-changing coastal areas, but to date has received wide recognition for its high accuracy (Babbel et al 2021; Bishop-Taylor et al. 2021).

### *3.3 Signal versus noise*

Major noise issues include afterpulses (and the system impulse response) and solar background signals. Here we describe these issues, as well as more minor issues of signal saturation and confidence flags. In the results section, we present sensitivity tests for removal of afterpulse/impulse response and solar background.

#### *3.3.1 Afterpulses and impulse response*

Subsurface photon returns are affected by the system impulse response function and afterpulsing. The impulse response function is essentially the signal which the instrument would receive from a perfectly reflective surface. In ocean water-column data, this is manifest as a diffuse cloud of photons typically occurring 20-40 m below the water surface (Fig. 2D, lower left). Afterpulses are strong peaks in photon counts which are the result of the laser signal reflecting off of surfaces within the laser receiver. Because these artifacts create a signal at distinct times, in the photon cloud they are translated into peaks at distinct depths of 2.3 m and 4.2 m below the ocean surface and sometimes deeper intervals (see Lu et al., 2021a, b). While impulse response and afterpulse artifacts are generally not problematic for studies of ice sheet surface elevations or seabed bathymetry, they create problems for studies of the water column and vegetation canopy heights because they contaminate the signal in areas of interest (i.e., within a few meters of the water or canopy surface). In the ocean, the strongest gradients in both light and photon attenuation often occur within several meters or tens of meters of the surface (depending on the water clarity), which means that the afterpulses in particular may lead to an unacceptable amount of distortion of the $K_{dph}$ signal due to natural particulates. For open-ocean studies (e.g., where plankton are of interest), it may be suitable to exclude the upper few meters of the water column to avoid the afterpulses (see Lu et al., 2020, 2023)—in coastal waters, though, the upper few meters may represent the natural zone where most of the $K_{dph}$ signal is attenuated, and so discarding this data means excluding the segment from any analyses.

In theory, the impulse response and afterpulse artifacts could be deconvolved from the signal if a pure response (devoid of any other natural signals) was known. Returns from the Salar de Uyuni salt flats in Bolivia (known as the flattest place on earth) have been used to isolate the impulse response and afterpulse signals (Martino, A., personal communication). However, deconvolution of these artifacts from natural signals is difficult because the "system response" (the impulse response plus afterpulses) is nonlinear and recursive, and one cannot remove it simply by dividing or subtracting the observed signal by the known system response or using a basic linear deconvolution from a standard signal processing toolbox. Another problem with deconvolution is that small errors can be very unforgiving. For the situations considered in this study and by others, implementing deconvolution analytically with a matrix did not remove afterpulse effects as intended, likely due to small variations in the width of the observed afterpulse peaks (Lu et al., 2021a,b). The process of designating a surface altitude and discretizing photons into vertical bins (which is a common processing strategy) also reduces the ease with which a matrix deconvolution can be implemented, because vertical alignment and width of the afterpulse peaks in the signal and impulse response function is essential. We note that the afterpulse peaks are also non-Gaussian, so Guassian decomposition methods are not ideal.

In this study we test two approaches concerning the afterpulses and impulse response:

(1) Subtracting the afterpulse peaks after identifying them through a fourth-order Gaussian decomposition. Even though the peaks are not fully Gaussian, this may be an adequate mitigation method.
(2) Doing nothing, on the premise that the afterpulses will have little effect on the slope of the exponential decay curve, and the idea that the impulse response is usually deeper than the signal of interest (and also small in magnitude)

For the first approach, we attempted to define an "ideal" set of Gaussian noise curves using a ~25-km section of nighttime data from coastal North Carolina during a period when low-turbidity conditions were present (Fig. 4A). These data were binned across the entire ~25-km subsegment at 0.05 m vertical resolution. After removing the surface peak manually, a four-part Gaussian decomposition was applied using a standard Matlab toolbox, and the resulting curves of photon counts were normalized to a 1-km standard along-track distance (Fig. 4C). The two afterpulse peaks and impulse response peaks were then subtracted from the case study datasets after binning them to 1-km horizontal distances and removing the solar background.

In the future, it may be desirable to use quality flags to remove problematic photons before binning the data. An updated quality flag in development for the Version 007 release of ICESat-2 data, which adds more detailed flagging to identify any photon in a nearly or fully saturated pulse, where it is detected in the return (surface, afterpulse, impulse response), and includes minor bug fixes. In version 006 of the data release (which are used throughout the rest of this study), this flag does not correctly identify all problematic photons, as seen in the Cook Inlet example in Fig. 2C. In the updated algorithm, the surface peak, afterpulses, and impulse response are more reliably flagged using *quality_ph* values 10-12 and 20-22 in pulses that are nearly and fully saturated.

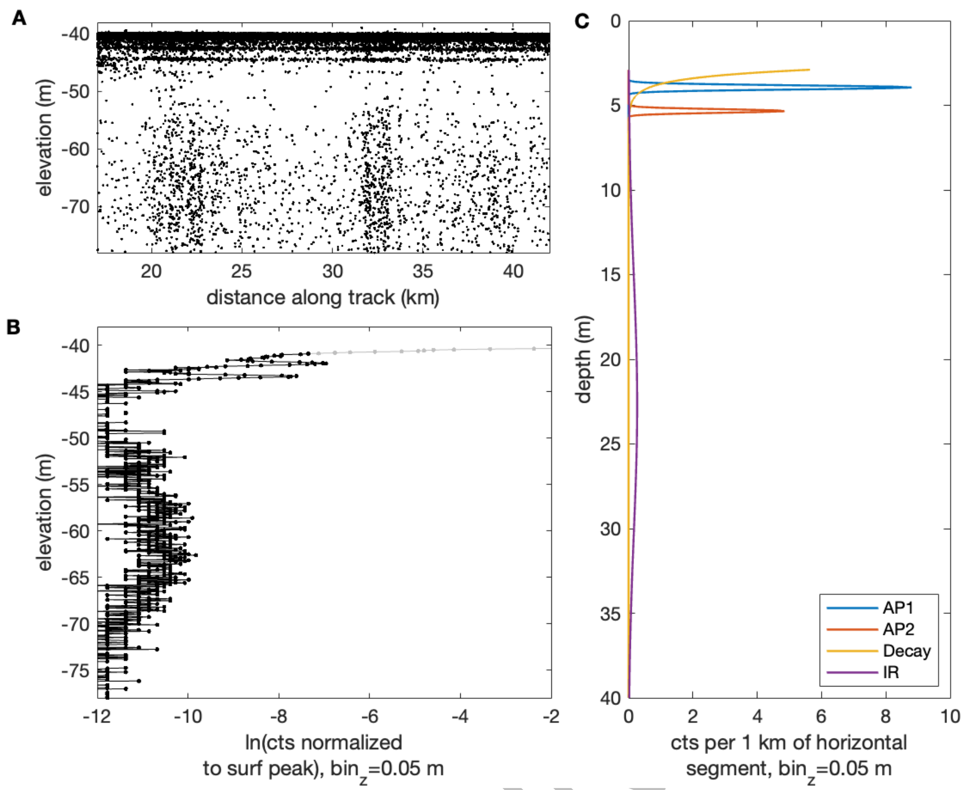


**Figure 4.** Example line showing strong afterpulses and impulse response. A) Subsegment from coastal North Carolina (track 1010). B) Data binned at 25-km horizontally and 0.05-m vertically. Note that data near the surface (shown in gray) were not included in the Gaussian decomposition in (C). C) Results of four-part Gaussian decomposition normalized to a 1-km horizontal distance.

### *3.3.2 Solar background*

Excessive contamination from solar background may present an issue for estimates of $K_{dph}$ from returns corresponding to positive solar angles. Solar-generated photons enter the laser receiver together with instrument-generated photons, to a degree which depends on solar angle and reflection from the surface (e.g., Markus et al., 2017; Neuenschwander and Magruder, 2019). These extraneous photons contaminate the atmospheric as well as the water-column signal (e.g., Fig. 2D; Lu et al., 2021b). This has led some researchers to neglect daytime data altogether (Lu et al., 2020, 2022; Eidam et al., 2022). Here we evaluate daytime returns for $K_{dph}$ after removing the solar background in an effort to determine if these data can be salvaged.

The solar background count rate is reported for a large vertical column (usually 500 m or more) of atmosphere within each ATL03 segment in the metadata structure. For consistency with the subsurface photon bins and solar background, the background count rate (*/beam/bckgrd_atlas/bckgrd_counts_reduced*) must be normalized by the height (*/beam/bckgrd_int_height_reduced*) used to generate it, as in Gibbons et al., (2021). The resulting solar background count rates are then reported with units of m$^{-1}$, which can be further normalized to generate background count rates for sub-meter vertical resolutions. The directory */bckgrd_atlas/*

provides reference latitudes and longitudes that are binned in the along-track direction, which means the solar background rate can be interpolated onto the same resolution of the latitude in the photon height (*/beam/heights/lat_ph*) for direct comparison. An alternate approach is to prompt the user to select a portion of atmosphere which corresponds to the water region of interest, and calculate a solar background rate at the same horizontal and vertical resolution as the water-column data. In this study we perform sensitivity tests to determine if daytime data can be used to generate meaningful $K_{dph}$ values.

#### *3.3.3 Signal versus noise and confidence flags*

ATL data are pre-processed to identify signal photons versus background (noise) photons using histograms of data binned at 280-m resolution along-track and 30 m vertically (Neumann et al., 2019). This method is helpful when locating the ground or water surface (e.g., Magruder et al., 2012). The results are classified into a confidence flag which is subdivided into five possible surface types for every photon return (/gtx/heights/signal_conf_ph). For example, photons are assigned a value of 4 (“high” confidence) if SNR>=100. That value may be assigned to more than one of the five surface type rows in the confidence variables (the surface type identifications are not always reliable, and not used in this study - we use a land mask instead to isolate surface waters, as noted in Section 3.1). We neglect the confidence variable in this study, because noise or background values typically constitute just a few percent of the photons in any given subsegment. We instead choose to manually remove the solar background and use quality flags to address afterpulses and impulse response (see Section 3.3.1).

In the ocean subsurface (within the water column), it may also be advantageous to normalize photon counts to the strength of the surface peak (e.g., Lu et al., 2020, 2023). Because the surface peak itself seems to represent a form of noise (see section 3.4), in this study we neglect this normalization, and instead rely on the exponential decay of the depth-corrected signal - absent any SNR threshold correction - to calculate an attenuation coefficient.

### 3.4 Identifying and excluding the surface peak

The ATL03 geolocated photons captured along track over the ocean clearly illustrate that the sea surface is the dominant reflector. This is evident in histograms of photon counts versus photon elevations, where the ocean surface signal is several orders of magnitude larger than the subsurface signal. This contrast exists for vertical histogram bin sizes on the order of 0.1 m to 1 m.

Numerous studies have employed various methods to identify the water surface peak based on ATL03 data (Lu et al. 2020; Thomas et al. 2022). Upon the identification of the surface peak, to exclude the impacts from surface peak, a common method is the omission of the first one or more meters of the water column beneath the peak (e.g., Lu et al., 2020, 2023; Corcoran and Parrish, 2021). However, in coastal waters, this approach may result in loss of most of the attenuation data, if the attenuation coefficient is large. It is thus important to explore the sensitivity of $K_{dph}$ estimates to the exclusion depth after surface peak detection. Following the methodology by Thomas et al, (2022), we identified dense clusters of photons around a height of 0 m as the surface photons, and subsequently used the median height of the detected surface photons to determine the surface peak (Thomas et al. 2022). This approach is sensitive to the vertical bin size. In this study, we used this approach with vertical bin sizes of 0.1 m, 0.5 m, and 1 m (see Section 3.7). Once the peak was identified, we implemented simple exclusion depths of 0.5, 1 and 2 m below the peak. This can be done after binning the data in the along-track distance (Section 3.7), or before (e.g., Fig. 5).

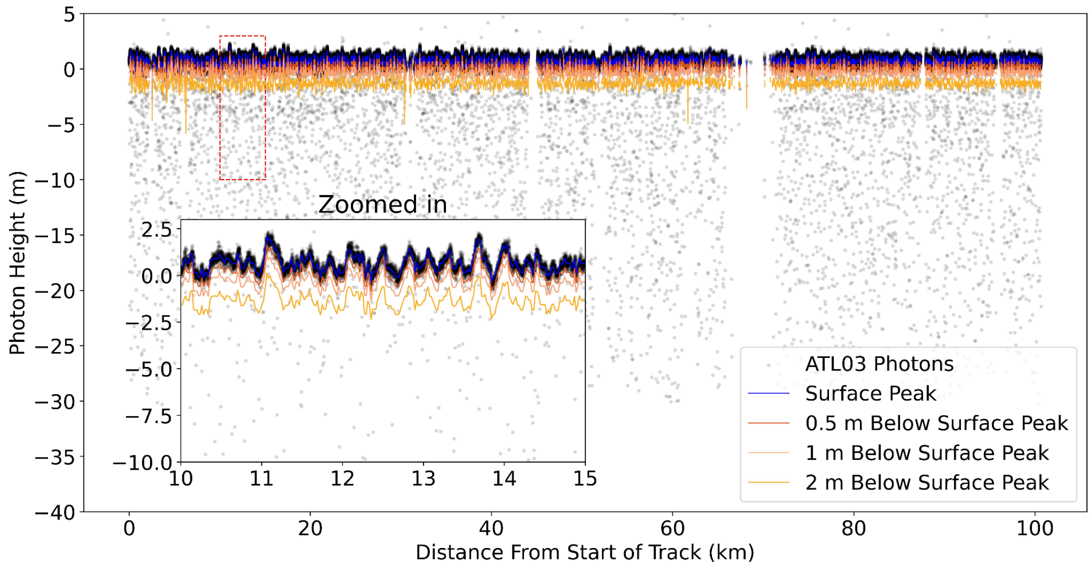


**Figure 5**: Example for Fixed Depth Exclusion of 0.5, 1 and 2 m below the surface peak for the Track 0472, east side of Hawai'i.

### 3.5. Refraction correction

Because light is refracted in water, the *z*-locations of photons are distorted in water relative to air. This problem has been explored in detail by researchers seeking to leverage ICESat-2 seabed returns for bathymetry data (e.g., Parrish et al., 2019; Ma et al., 2020; Babbel et al., 2021; Thomas et al., 2021). Parrish et al. (2019) provide a generalized correction equation:

$$Z' = Z + 0.25416D \qquad \text{(Eq. 1)}$$

Where $Z$ is the elevation of a photon as reported in the ATL03 data structure, $D$ is the water depth of the photon below the sea surface, and $Z'$ is the corrected depth. Because elevations are positive upward, this means that the corrected photon elevations are ~25% shallower than the raw reported elevations, from a bathymetric perspective. In practice this correction can be applied to raw photon elevation data after the elevation of the surface peak has been found. If the surface peak is determined using a histogram approach (see section 3.4), this requires an iterative approach. In other words, first bin the data horizontally and vertically to determine where the water surface is within a given section; then use that surface elevation in Equation 1 to correct all of the raw photon elevations. Finally, re-calculate the histogram using these adjusted photon elevations.

### 3.6 Other corrections and issues to consider

While the processing steps in sections 3.1-3.5 address a variety of common data issues, users should take care to evaluate other possible issues with their site of interest. For example, while the signal extinction depth of ATLAS is commonly less than the bathymetric depth, in shallow coastal waters bathymetry may be visible. A robust seabed-detection approach may be required in order to efficiently isolate the water column. Presently there are a few routines available (e.g., Markel et al., 2023; Parrish et al., 2019; Thomas et al., 2021). In such environments, it is also unclear to what degree bottom reflection may contaminate the signal, and users are advised to do comparisons with in situ measurements of $K_{dph}$ or some other sensitivity test to determine if excess photons are present in the water column which may lead to an under-estimate of the attenuation term.

In some ICESat-2 applications, vertical datum corrections are important. Here, we suggest that because the attenuation in water is independent of any absolute sea-surface height, it is sufficient to simply normalize the depth-in-water column to the relative sea-surface height within a single subsection. As such, within the water column we have applied a simple linearly scaled refraction correction (Eq. 1), but more elaborate approaches may be desired (see Parrish et al., 2019).

Beam strength and beam position within the array are also issues to consider. Strong beams generate ~3-4 times more photon returns than the weak beams due to the higher laser power (e.g., Neumann et al., 2019). While some researchers have suggested combining the data within each strong-weak beam pair to provide better data density in the ocean subsurface (e.g., Corcoran and Parrish, 2021), this may not be a suitable approach in shallow coastal systems where the sea surface and seabed are changing over short spatial scales (due to waves and irregular bathymetry, respectively) and where turbidity gradients are strong. In other words, the turbidity field may change even across the 90-m spacing of the strong and weak beams, e.g., in a river plume. In more open ocean waters, however, combining data may be very reasonable.

Differences in signal return from the nadir versus outer beams may also result in variations in photon returns and/or saturation values (due to differing angles of incidence on the sea surface). We briefly explored saturation differences between beam pairs, but did not find notable differences - though the center weak beam generally has the most issues with saturation. It is generally good practice to discard fully saturated pulses, because the effects on the data are not well-constrained in terms of photon height accuracy, radiometric corrections, first photon bias, etc.

ATL data have been used to successfully measure heights of surface waves in the ocean, which presents a novel and valuable application of ICESat-2 (e.g., Klotz et al., 2019; Horvat et al., 2020). However, for $K_{dph}$ calculations, surface waves are problematic because they effectively widen the surface peak, meaning that more data must be discarded from the surface than in cases of calm seas. This problem is exacerbated when combining beam pairs, because the wave field may manifest as different shapes across the 90-m beam separation distance. Sometimes this can result in a double surface peak in histograms which confuses the surface-detection algorithm. An example of this problem is provided in Fig. 6, which depicts data from a 500-m subsegment of the Columbia River plume (RGT 0067, 2019-01-01, $bin_x$ = 500 m, $bin_z$ = 0.25 m; solar background has been removed). This type of problem could potentially be resolved by finding the mean surface elevation, segmenting the data into very small along-track distances, and adjusting the vertical position of photons in every interval up or down in elevation to match the mean surface - which would in effect flatten the surface. This may also introduce more noise to the data, however. Another approach is to calculate the kurtosis or similar measurement of peak width (as noted in Section 3.4) and use this to choose a larger surface-peak exclusion depth (e.g., more than 2 m for the example shown in Fig. 6B), or as a filter to reject these segments from $K_{dph}$ calculations altogether.

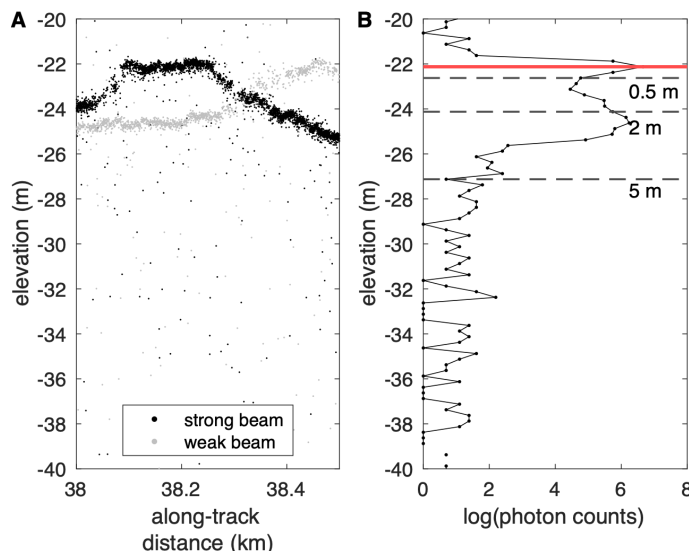


**Figure 6**. Example of problems generated by surface-gravity waves (ocean waves). A) Photon clouds from the strong and weak beams, which both exhibit surface waves with heights of >1 m. B) Natural log-transformed histogram of photon counts for the combined data from the strong and weak beams, which exhibits a double surface peak. The red line denotes the surface as identified by the maximum value in the histogram, as well as possible surface cutoff values of 0.5, 2, and 5 m.

Finally, in the upper water column where attenuation signals are strongest, bubbles may also be present which could contaminate the signal. During periods of strong wind and wave breaking, bubbles plumes can extend several meters into the subsurface (e.g., Strand et al., 2020; Cifuentes-Lorenzen et al., 2023). It is unclear to what degree these may contaminate the ATL subsurface attenuation profiles. However, during these periods, it is also likely that there may be no ATL data available due to clouds. If skies are clear, the sea surface may also be so rough that calculating $K_{dph}$ is impractical because so much surface data must be removed (see above).

Relationships have been found between wind speed and bubble depth, and wave height and bubble depth (Thorpe, 1992; Wang et al., 2016). For future analyses of $K_{dph}$ in natural waters, some consideration of both wind speed and wave height is recommended, and the impacts on bubble impacts on the $K_{dph}$ signal may warrant a targeted study, for improved signal cleaning (or even for studies of bubbles). Details of this issue are not explored in this work, but may be a useful topic for future research.

### 3.7 Horizontal and vertical binning

For attenuation calculations, photon XYZ data are commonly "binned" (or aggregated or subsetted) in the along-track ($x$) dimension (e.g., Lu et al., 2020, 2023; Corcoran and Parrish, 2021). Larger bin sizes produce data subsets with a larger number of points, which can be advantageous for improved quality of the attenuation signal. However, binning over larger distances can also introduce unwanted artifacts or complexities in the data. For example, in coastal waters, a horizontal bin size of 2 km may include water masses characterized by different particulate loads, may include regions of varying seafloor bathymetry (which may impact seabed reflectivity per Section 3.6), and may encompass regions of differing turbidity or afterpulse character (Figs. 2B, 2C). Smaller bin sizes (e.g., 500 m) may be advantageous in areas where particulate loading is higher and/or much natural variability (e.g., in bathymetry or water-mass properties) occurs over small spatial scales. Along-track bin sizes as small as ~7 m have been used in plankton studies (Lu et al., 2020). However, in open-ocean waters, using larger bins may be advantageous to provide better data density where particles are sparse. Here we tested horizontal bin dimensions of 500 m, 1000 m, and 2000 m for each of the four sites.

Vertical binning of photon data is also key in calculating attenuation coefficients. Like the horizontal binning, this choice should also be made on the basis of the density of available photon data. Larger bins will provide better data density in each bin, but at the expense of vertical resolution. Smaller bins should improve vertical resolution up to a point at which noise becomes excessive. Much like the horizontal bin size, choice of vertical bin size depends on whether the environment has high or low particle loading and spatial variability. Vertical bin sizes of 0.1 m, 0.5 m, and 1 m were tested here.

### 3.8 Fitting an exponential decay curve

Once data have had suitable corrections applied, an exponential decay curve can be fit to the data based on the Lambert-Beer Equation (or "Beer's Law"):

$$E_z = E_0 e^{-K_d z} \qquad \text{(Eq. 2)}$$

Where $E_0$ is the downwelling irradiance entering the water (μmol m$^{-2}$ s$^{-1}$), $K_d$ is the diffuse attenuation coefficient, and $E_z$ is the irradiance (μmol m$^{-2}$ s) at depth $z$ (m). In practice, this can be applied using a linear regression to the histogram of depth versus log-transformed photon counts within the water column according to the following equation:

$$\ln(E_z) = -(K_{dph} z) + \ln(E_0) \qquad \text{(Eq. 3)}$$

Where $E_0$ is the incoming photon "intensity" just below the surface (photon counts per bin), $E_z$ is the photon intensity (photon counts per bin) at depth $z$ (m), and $K_{dph}$ is the photon attenuation coefficient (m$^{-1}$). Because the surface peak represents a strong reflection of photons from the water surface, it does not seem valid to use the number of photon counts in the surface layer for $E_0$. Here we recommend removing the surface peak entirely before calculating $E_0$ or $E_z$ (see section 3.4).

In practice, a large value of $K_d$ (e.g., >1) represents high attenuation (e.g., because of turbid water and/or high colored dissolved organic matter) while a small value of $K_d$ (e.g., <<1) represents low attenuation and relatively clear water.

**3.9 Evaluation of results - do they make sense?**

It is relatively easy to fit an exponential decay curve to subsurface photon data and generate an attenuation coefficient. Determining if the derived value is a good representation of subsurface SSC, CDOM, plankton, etc. is more difficult. In this study we compare derived $K_{dph}$ values from sites in the Pacific and Mediterranean to data from Argo gliders (https://argo.ucsd.edu/) to determine if there is a good match. For other sites we evaluate the range of $K_{dph}$ values against general studies of attenuation in similar types of environments, and leave further validation for a future study.

**4. Results of sensitivity tests**

Sensitivity tests were performed to address afterpulse/impulse response removal (per section 3.3), solar background removal (per section 3.3), horizontal and vertical bin sizes (per section 3.7), depth of surface peak exclusion (per section 3.4), and beam pairing (per section 3.6). Results are presented here and are summarized and synthesized into a suggested workflow in section 5.

**4.1 Afterpulse and impulse response removal**

Gaussian peaks representing the first two afterpulses and the impulse response were calculated as described in Section 3.3.1 using data from North Carolina ($bin_x$ = 1 km, $bin_z$ = 5 cm). These data were subtracted from the photon histograms for nighttime Cook Inlet case study (Fig. 2B, C; $bin_x$ = 1 km, $bin_z$ = 5 cm, solar background removed). This case study was chosen because it exhibited the strongest afterpulse signals. The solar background was removed and the depths were corrected for refraction in the pre-processing stage. Because gaussian peaks derived from the North Carolina dataset were taller than the peaks observed in the Cook Inlet data, they were scaled by a factor of 2 before subtraction. After peak subtraction, any photon counts which were negative were assigned null values.

The $K_{dph}$ values calculated from the cleaned photon clouds were generally less than the values calculated from the full photon clouds (Fig. 7). This suggests that where afterpulses are present, they may bias the results toward slightly higher $K_{dph}$ values if not removed - however, this approach represents a fairly crude method which can likely be improved through better quality flagging in future Version 007 and subtraction of photons prior to the generation of histograms.

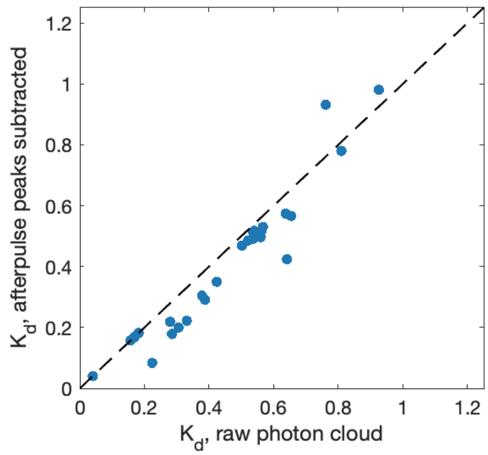


**Figure 7**. Sensitivity test results for afterpulse removal. (The impulse response was removed as well, but is generally below the zone where the attenuation profile can be detected.) Removal of afterpulses generally resulted in lower $K_{dph}$ values.

## 4.2 Solar background removal

The solar background rate was relatively high for the daytime Cook Inlet and Baja examples and relatively low for the nighttime examples (Fig. 2C-F, Table 1). Values of $K_{dph}$ were calculated for the daytime examples before and after removing the solar background. For the Cook Inlet example, $K_{dph}$ values with and without the background were very small and not considered appropriately representative of $K_d$ values expected for a muddy embayment. For the Baja example, $K_{dph}$ values were slightly greater when the solar background was excluded. It is worth noting there that for the nighttime datasets, solar background did not impact $K_{dph}$ because the background rates were less than 0.5 m$^{-1}$ when binned along-track at 1 km (Table 1). Since the rate is rounded to the nearest whole integer for subtraction from the histogram, it disappeared from the datasets.

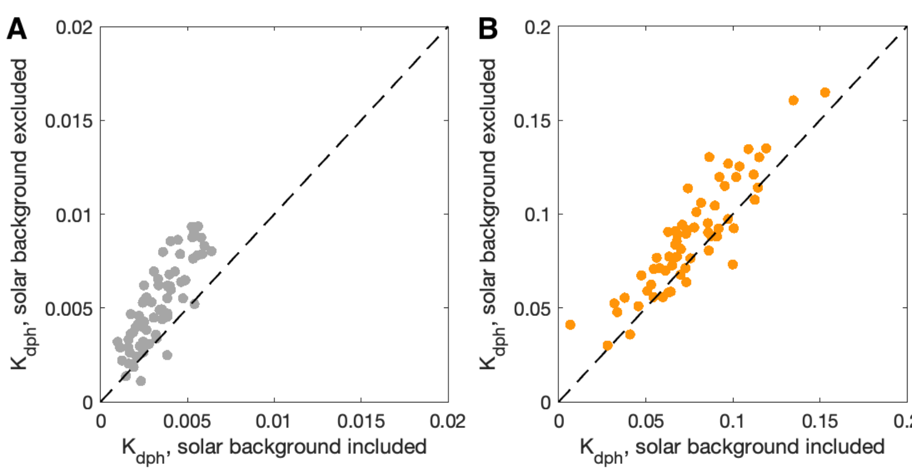


**Figure 8**. Result of solar-background sensitivity test for A) Cook Inlet daytime example (track 0632; Fig. 2D) and B) Baja daytime example (track 0341; Fig. 2F).

### 4.3 Horizontal and vertical bin sizes

The choice of bin size impacted the $K_{dph}$ values, resulting in differences of approximately 5-15% (Fig. 9). The effect was more pronounced with the choice of vertical bin size (Fig. 9B). Specifically, $K_{dph}$ values derived from 1.0-m bins were, on average, ~13% higher than those computed from 0.25-m bins. In contrast, the influence of horizontal bin sizes was less notable, and $K_{dph}$ values calculated based on 2000-m versus 500-m binned data were fairly comparable (Fig. 9A). However, some low-value outliers from the Rio de la Plata and Cook Inlet samples led to an overall ~5% reduction in $K_{dph}$ values for the larger horizontal bin sizes. This can be attributed to the turbid water of these coastal areas that exhibit strong spatial gradients. Utilizing larger bin sizes in such regions creates a sort of dilution effect, where lower-turbidity waters are aggregated with higher-turbidity waters.

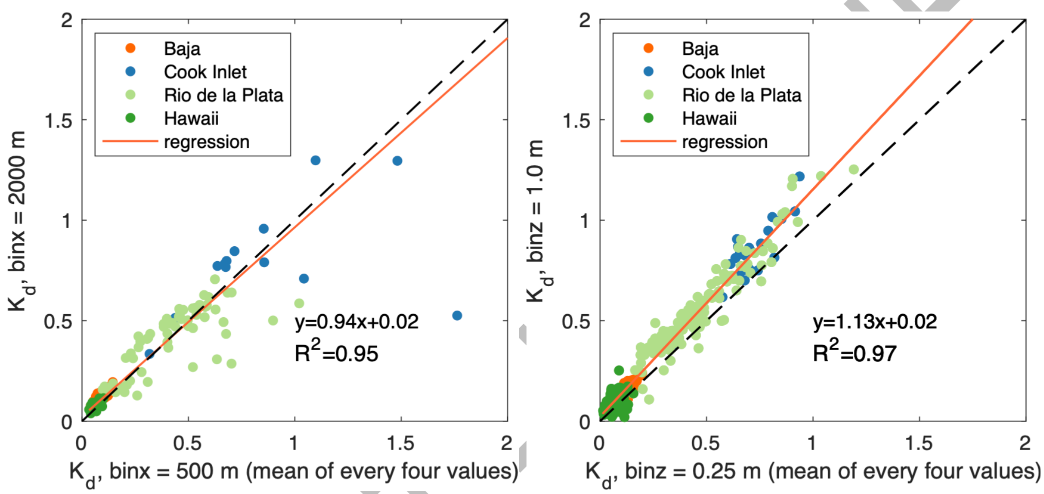


**Figure 9**. Results of bin-size sensitivity tests. A) $K_{dph}$ for 2000-m horizontal bins versus 500-m horizontal bins. Larger bins tend to generate slightly higher $K_{dph}$ values, but a few outliers from the Rio de la Plata and Cook Inlet examples (which are both relatively muddy systems) biased the results toward slightly lower $K_{dph}$ values for larger bins (~5% lower). B) $K_{dph}$ for 1.0-m vertical bins versus 0.25-m vertical bins. Larger vertical bins generated $K_{dph}$ values that were on, on average, 13% higher than for smaller bins.

### 4.4 Depth of surface peak exclusion

Given the potential for residuals of the ocean surface signal to contaminate the subsurface signal, we assessed $K_{dph}$ calculation results obtained by removing signals at two distinct depths: 1.0 m and 0.5 m below the sea surface peak (Fig. 10). Excluding a larger surface depth (1.0 m) resulted in $K_{dph}$ values that were ~17% lower than those calculated using a 0.5-m surface depth exclusion.

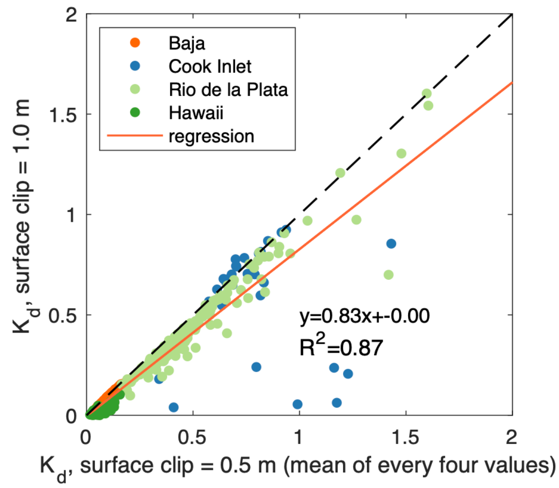


**Figure 10**. $K_{dph}$ results for surface peak removal to 1.0-m depth versus to 0.5-m depth. Excluding a larger portion of the surface (1.0 m) resulted in $K_{dph}$ values that were ~16% lower than for a smaller portion (0.5 m).

### 4.5 Beam pairing

Different $K_{dph}$ were calculated for paired versus unpaired beams, but these results largely reflected the difference in $K_{dph}$ obtained from strong versus weak beams (Fig. 11). $K_{dph}$ calculated from strong beams were ~6% higher than values calculated from weak beams, though there was considerable scatter in the data (Fig. 11A), especially for Rio de la Plata and Baja California. This may be a function of strong spatial gradients (vertically and horizontally) in particulates. Values of $K_{dph}$ calculated from paired beams were slightly higher than values calculated from strong beams, though some outliers biased the linear regression toward a slope less than one (Fig. 11B). Values of $K_{dph}$ calculated from paired beams were notably higher than for weak beams (which, as noted above, reflected the strong-weak beam relationship).

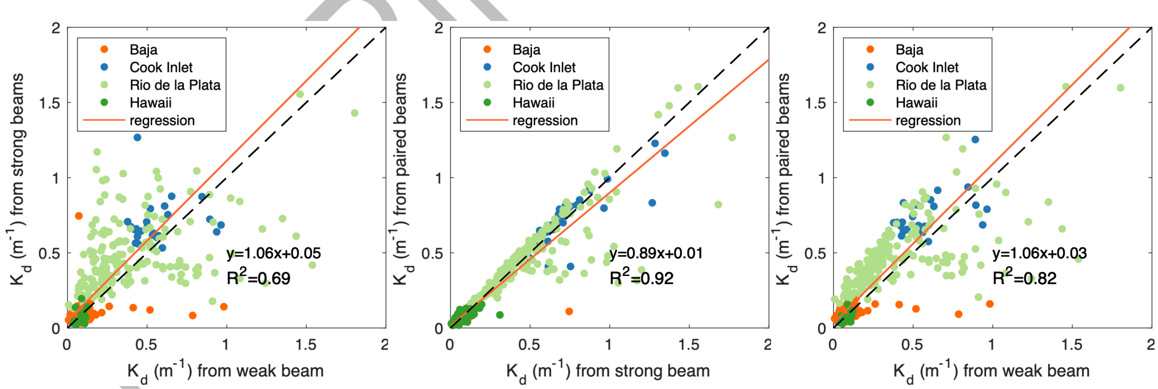


**Figure 11**. Results of sensitivity tests for paired beam and single-beam data. A) $K_{dph}$ from the strong beams versus $K_{dph}$ from the weak beams. There was much scatter in the data but results from strong beams were on average 6% higher than from weak beams. B) $K_{dph}$ from the paired beams versus $K_{dph}$ from the strong beams. Paired-beam $K_{dph}$ values were fairly comparable to strong-beam $K_{dph}$ values, but outliers (primarily in the Rio de la Plata and Cook Inlet examples) biased paired-beam data to values lower than the strong-beam data. C) $K_{dph}$ from the paired beams versus $K_{dph}$ from the weak beams. Paired-beam $K_{dph}$ values were ~6% greater than weak-beam $K_{dph}$ values.

## 5. Discussion

### 5.1 Lessons learned from sensitivity tests

Based on the sensitivity tests, $K_{dph}$ values calculated from ATL03 data may vary by up to ~30% depending on what processing choices are made concerning some commonly recognized issues and artifacts in the data. Removal of solar background generated the biggest difference (30%), but the lack of scatter in the $K_{dph}$ values pre- and post-background removal (Fig. 8) suggests that daytime data may be usable for $K_{dph}$ calculations. The remaining processing choices of bin sizes, surface peak removal, and beam pairing all had smaller impacts of the data, and caused variations in $K_{dph}$ across datasets of only ~6-17%. This is encouraging because it means that even where in situ validation data are absent, useful $K_{dph}$ results may be obtainable, and may be better interpretable using the sensitivity tests presented above.

The results above do highlight some nuanced decisions which users should make when considering different sites. For example, in highly turbid waters with strong vertical and horizontal gradients in suspended particle distributions (Fig. 2B-D), it may be wise only to use the strong beam data. In these cases, the $K_{dph}$ values calculated from weak-beam data exhibited considerable scatter relative to the values calculated from the strong-beam data (Fig. 11A). In these waters, using the strong-beam data is intuitive because there should be better signal penetration and thus a better-quality attenuation profile in waters where particulates are scattering and absorbing much of the signal. For environments where large waves are present (e.g., Fig. 6), it may be desirable to exclude a larger surface peak, but users should be aware that this will bias the $K_{dph}$ results toward lower values (Fig. 10). Finally, while horizontal bin sizes seemed to have little impact on the results, larger vertical bin sizes tend to bias the $K_{dph}$ results toward higher values. Larger vertical bins may be desirable in waters with low particle loads (e.g., Hawaii), but in highly turbid waters (e.g., Cook Inlet and Rio de la Plata), smaller vertical bin sizes may be necessary in order to obtain a usable attenuation profile. Vertical bins may also be a factor in how afterpulses are treated (see Section 3.3.1), and thus bin sizes should be selected with care.

The issue of afterpulses remains a challenge. Developing idealized Gaussian peaks which represent the afterpulses is not ideal because the peaks must be carefully aligned with each dataset in question in the vertical dimension prior to subtraction, and the magnitude must also be manually tuned in an effort to fully eliminate the noisy data. Ideally the new quality flags being developed for Version 007 of the ALT03 data will allow for easy deletion of afterpulse photons. Additionally, photon weights (categorized under the *weight_ph* variable) may be refined in such a way as to help identify problem photons which are not flagged by *quality_ph*. In this study, attenuation profiles used for $K_{dph}$ calculations typically spanned less than 10 m of the upper water column, and so the impulse response does not seem to be a major issue for this type of analysis.

### 5.2 Evaluating the quality of results

With the exception of the daytime results, the $K_{dph}$ patterns observed at each site are reasonable based on comparisons with Sentinel satellite images (Fig. 12). Lower $K_{dph}$ values correspond to clearer waters, and higher $K_{dph}$ values correspond to regions with higher sediment and/or chlorophyll content (Fig. 12). Furthermore, values in the clearer Baja California (Fig. 12A) are approximately an order of magnitude lower than values in the muddier Rio de la Plata (Fig. 12B). This is a useful result because it means that while passive remote sensing products such as Landsat, MODIS, and Sentinel can give information about spatial variability in particle loading and CDOM during the day, ICESat-2 can provide additional information at night.

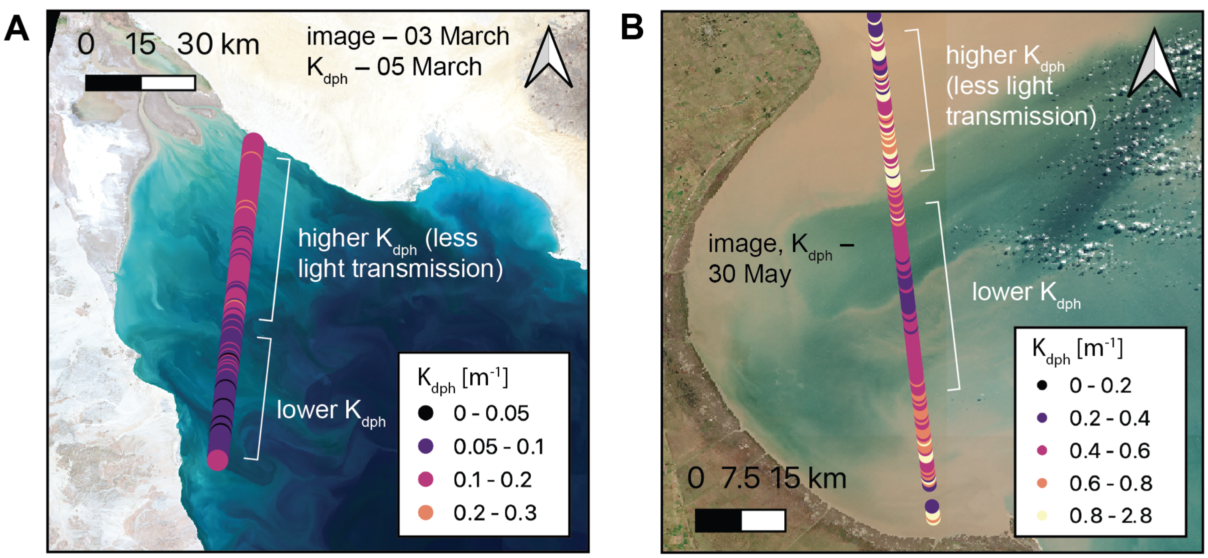


**Figure 12**. Overlays of $K_{dph}$ results on Sentinel-3 satellite images. A) Baja California, GT1141 (image is two days older than Kd results). B) Rio de la Plata estuary, GT1039. Note that in both cases daytime images are displayed but nighttime $K_{dph}$ results are presented — thus some differences in spatial patterns between ATL $K_{dph}$ results and Sentinel images are expected (see Table 1).



While ATL products thus appear to provide useful information about spatial variability in $K_{dph}$, there is greater utility in being able to quantify $K_{dph}$ and use it as an effective proxy (or scalable proxy) for a more common attenuation parameter like $K_{dPAR}$. To assess this, a subset of $K_{dPAR}$ measurements from ARGO gliders were extracted which coincided loosely with ICESat-2 flyovers in space in time—i.e., within 200 m horizontally and within +/- 24 hours. The sites used were in the central Pacific and in the Mediterranean off the east coast of Italy. Only nighttime ICESat-2 lines were used to avoid solar background issues. For each site, 12–93 Kdph values were matched to a single ARGO measurement. Values of Kdph ranged from ~0 to 0.2, and were generally somewhat higher than the ARGO measurements, though the ARGO $K_{dPAR}$ values fell within the range of each $K_{dph}$ dataset (Fig. 13). While more extensive validation is warranted in a future study, this comparison offers promise for $K_{dph}$ being a useful proxy for $K_{dPAR}$ and possibly other attenuation products like $K_{d490}$ (a common product of passive remote sensing images).

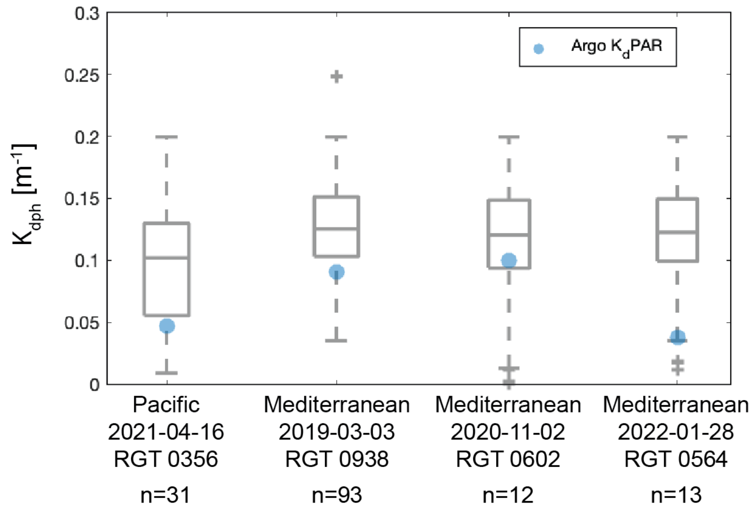


**Figure 13**. Comparisons between $K_{dph}$ and Argo $K_{dPAR}$ data. Box plots illustrate the range of $K_{dph}$ values within 210 meters (horizontally) of the Argo $K_{dPAR}$ value at each site (each $K_{dPAR}$ value is shown in blue). The number of $K_{dph}$ datapoints represented in each box plot is shown below the x-axis.

### 5.3 Suggested workflow

The workflow for calculating $K_{dph}$ will vary by user and application, but a general outline is proposed in Fig. 14. This is designed to be converted into a cloud-compatible toolbox in an upcoming effort. Note that the depth correction is necessarily iterative, because histograms must first be created in order to identify the depth of the surface peak (which is used as the reference for the depth correction) and then the histogram must be re-calculated using the corrected depths. Users may wish to add processing steps to this workflow.

## 6. Conclusions

This study presents processing considerations and sensitivity test results for calculating $K_{dph}$ from ICESat-2 ATL03 data. The processing choices explored in this study resulted in $K_{dph}$ differences of ~6-17%, and examples from the Pacific and Mediterranean encompassed $K_{dPAR}$ values measured by ARGO floats. While this range warrants some tuning and further exploration through studies of different case studies, it also indicates that $K_{dph}$ from ICESat-2 data may be quite useful in waters ranging from clear open-ocean sections to turbid coastal sections. Removal of afterpulses remains an ongoing challenge that will likely be easier to address in future ATL data versions. Dealing with large surface waves will require additional tuning, and some daytime data may be salvageable given a carefully constructed filter for data quality. Remaining issues, however, should be relatively straightforward to address by using the sensitivity tests presented here as a guide.

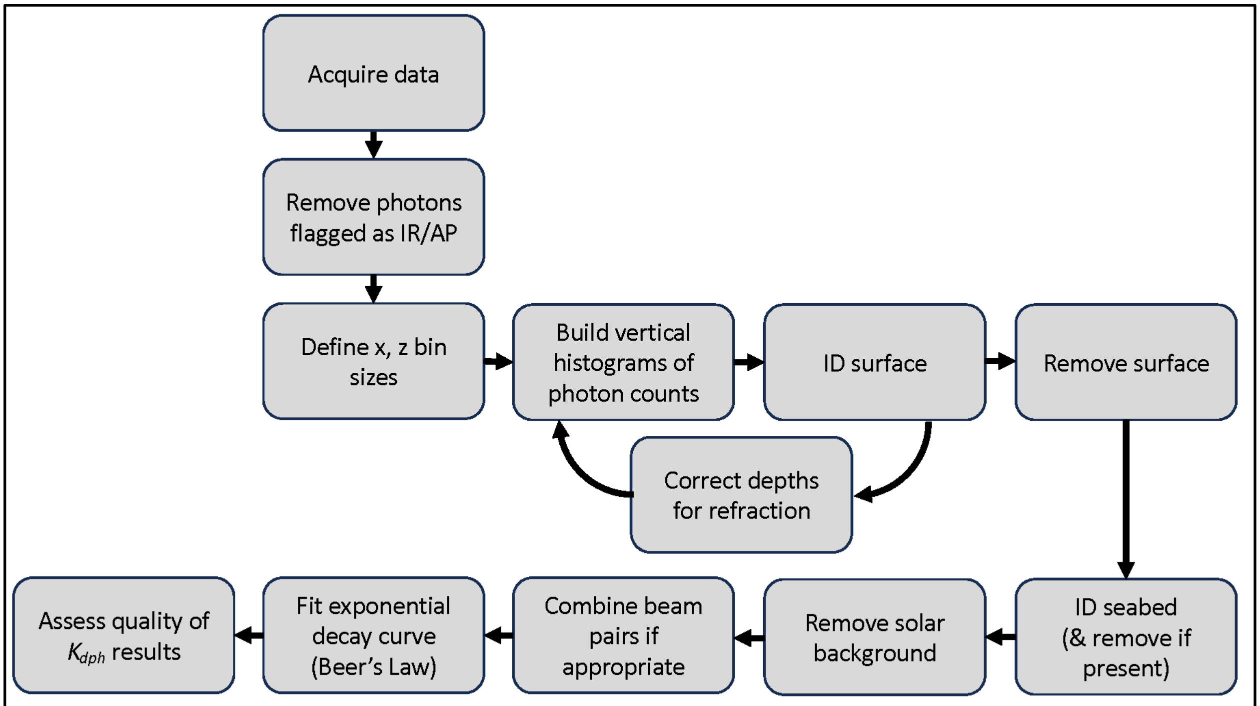


**Figure 14**. Suggested workflow for calculating $K_{dph}$ from ATL03 data.



**Acknowledgments:**

This work was funded by NASA award 80NSSC21K0914, 80NSSC20K0970, and Oregon State University. The authors wish to thank Jonathan Markel, Dr. Chris Parish, and Forrest Corcoran for discussions about bathymetric data detection, and Lillian Cooper and Matthew Paris for assistance in downloading the North Carolina datasets.

**Code accessibility:**

Codes used to calculate Kd from ATL .h5 files (available from the NASA EarthData portal) are available on GitHub at: https://github.com/emilyeidam/icesat-2_kdph.

**References:**

Acker, J., Ouillon, S., Gould, R., Arnone, R. (2005). Measuring marine suspended sediment concentrations from space: history and potential. In *8th International Conference on Remote Sensing for Marine and Coastal Environments, Halifax, NS, Canada*.

Babbel, B. J., Parrish, C. E., & Magruder, L. A. (2021). ICESat-2 elevation retrievals in support of satellite-derived bathymetry for global science applications. *Geophysical research letters*, 48(5), e2020GL090629.

Barnes, B. B., Hu, C., Kovach, C., & Silverstein, R. N. (2015). Sediment plumes induced by the Port of Miami dredging: Analysis and interpretation using Landsat and MODIS data. *Remote Sensing of Environment*, *170*, 328-339.

Behrenfeld, M. J., Gaube, P., Della Penna, A., O'malley, R. T., Burt, W. J., Hu, Y., ... & Doney, S. C. (2019). Global satellite-observed daily vertical migrations of ocean animals. *Nature*, *576*(7786), 257-261.

Behrenfeld, M. J., Hu, Y., Bisson, K. M., Lu, X., & Westberry, T. K. (2022). Retrieval of ocean optical and plankton properties with the satellite Cloud-Aerosol Lidar with Orthogonal Polarization (CALIOP) sensor: Background, data processing, and validation status. *Remote Sensing of Environment*, *281*, 113235.

Behrenfeld, M. J., Hu, Y., O'Malley, R. T., Boss, E. S., Hostetler, C. A., Siegel, D. A., ... & Scarino, A. J. (2017). Annual boom–bust cycles of polar phytoplankton biomass revealed by space-based lidar. *Nature Geoscience*, *10*(2), 118-122.

Bishop-Taylor, R., Nanson, R., Sagar, S., & Lymburner, L. (2021). Mapping Australia's dynamic coastline at mean sea level using three decades of Landsat imagery. Remote Sensing of Environment, 267, 112734.

Bisson, K. M., & Cael, B. B. (2021). How are under ice phytoplankton related to sea ice in the Southern Ocean?. *Geophysical Research Letters*, *48*(21), e2021GL095051.

Bisson, K. M., Boss, E., Werdell, P. J., Ibrahim, A., Frouin, R., & Behrenfeld, M. J. (2021a). Seasonal bias in global ocean color observations. *Applied optics*, *60*(23), 6978-6988.

Bisson, K. M., Boss, E., Werdell, P. J., Ibrahim, A., & Behrenfeld, M. J. (2021b). Particulate backscattering in the global ocean: a comparison of independent assessments. *Geophysical research letters*, *48*(2), e2020GL090909.

Cifuentes-Lorenzen, A., Zappa, C. J., Randolph, K., & Edson, J. B. (2023). Scaling the Bubble Penetration Depth in the Ocean. *Journal of Geophysical Research: Oceans*, *128*(9), e2022JC019582.

Collister, B. L., Zimmerman, R. C., Sukenik, C. I., Hill, V. J., & Balch, W. M. (2018). Remote sensing of optical characteristics and particle distributions of the upper ocean using shipboard lidar. *Remote Sensing of Environment*, 215, 85-96.

Corcoran, F., & Parrish, C. E. (2021). Diffuse Attenuation Coefficient (Kd) from ICESat-2 ATLAS Spaceborne Lidar Using Random-Forest Regression. *Photogrammetric Engineering & Remote Sensing*, *87*(11), 831-840.

Doxaran, D., Froidefond, J. M., Lavender, S., & Castaing, P. (2002). Spectral signature of highly turbid waters: Application with SPOT data to quantify suspended particulate matter concentrations. *Remote sensing of Environment*, *81*(1), 149-161.

Eidam, E., Walker, C., Bisson, K., Paris, M., & Cooper, L. (2022). Novel application of ICESat-2 ATLAS data to determine coastal light attenuation as a proxy for suspended particulate matter. In *OCEANS 2022, Hampton Roads* (pp. 1-7). IEEE.

Jamet, C., Ibrahim, A., Ahmad, Z., Angelini, F., Babin, M., Behrenfeld, M. J., ... & Zhai, P. W. (2019). Going beyond standard ocean color observations: lidar and polarimetry. *Frontiers in Marine Science*, 6, 251.

Klotz, B. W., Neuenschwander, A., & Magruder, L. A. (2020). High-resolution ocean wave and wind characteristics determined by the ICESat-2 land surface algorithm. *Geophysical Research Letters*, *47*(1), e2019GL085907.

Horvat, C., Bisson, K., Seabrook, S., Cristi, A., & Matthes, L. C. (2022). Evidence of phytoplankton blooms under Antarctic sea ice. *Frontiers in Marine Science*, *9*, 2154.

Lu, X., Hu, Y., Yang, Y., Bontempi, P., Omar, A., & Baize, R. (2020). Antarctic spring ice-edge blooms observed from space by ICESat-2. *Remote Sensing of Environment*, *245*, 111827.

Horvat, C., Blanchard-Wrigglesworth, E., & Petty, A. (2020). Observing waves in sea ice with ICESat-2. Geophysical Research Letters, 47(10), e2020GL087629.

Lee, Z. P., Darecki, M., Carder, K. L., Davis, C. O., Stramski, D., & Rhea, W. J. (2005). Diffuse attenuation coefficient of downwelling irradiance: An evaluation of remote sensing methods. Journal of Geophysical Research: Oceans, 110(C2).

Lu, X., Hu, Y., Yang, Y., Bontempi, P., Omar, A., & Baize, R. (2020). Antarctic spring ice-edge blooms observed from space by ICESat-2. Remote Sensing of Environment, 245, 111827.

Lu, X., Hu, Y., Yang, Y., Neumann, T., Omar, A., Baize, R., ... & Winker, D. (2021a). New Ocean Subsurface Optical Properties From Space Lidars: CALIOP/CALIPSO and ATLAS/ICESat-2. *Earth and Space Science*, *8*(10), e2021EA001839.

Lu, X., Hu, Y., Yang, Y., Vaughan, M., Palm, S., Trepte, C., ... & Baize, R. (2021b). Enabling value added scientific applications of ICESat-2 data with effective removal of afterpulses. *Earth and Space Science*, *8*(6), e2021EA001729.

Lu, X., Yang, Y., Hu, Y., Rogers, L., & Omar, A. (2022). Global Ocean studies from ICESat-2 mission. In *OCEANS 2022, Hampton Roads* (pp. 1-5). IEEE.

Lu, X., Hu, Y., Omar, A., Yang, Y., Vaughan, M., Lee, Z., ... & Getzewich, B. (2023). Lidar attenuation coefficient in the global oceans: insights from ICESat-2 mission.

Ma, Y., Xu, N., Liu, Z., Yang, B., Yang, F., Wang, X. H., & Li, S. (2020). Satellite-derived bathymetry using the ICESat-2 lidar and Sentinel-2 imagery datasets. *Remote Sensing of Environment*, *250*, 112047.

Magruder, L. A., Brunt, K. M., & Alonzo, M. (2020). Early ICESat-2 on-orbit geolocation validation using ground-based corner cube retro-reflectors. *Remote Sensing*, *12*(21), 3653.

Magruder, L. A., Wharton III, M. E., Stout, K. D., & Neuenschwander, A. L. (2012). Noise filtering techniques for photon-counting ladar data. In *Laser Radar Technology and Applications XVII* (Vol. 8379, pp. 237-245). SPIE.

Markel, J., Parrish, C., Thomas, N., Lowell, K., Lu, X., 2023. ICESat-2 Batymetry. GitHub Online Repository available online at https://github.com/ICESat2-Bathymetry/Information. Accessed 2023-08-31.

Markus, T., T. Neumann, A. Martino, W. Abdalati, K. Brunt, B. Csatho, S. Farrell, H. Fricker, A. Gardner, D. Harding, M. Jasinski, R. Kwok, L. Magruder, D. Lubin, S. Luthcke, J. Morison, R.

Nelson, A. Neuenschwander, S. Palm, S. Popescu, C. K. Shum, B. E. Schutz, B. Smith, Y. Yang, and J. Zwally. 2017. The Ice, Cloud, and land Elevation Satellite-2 (ICESat-2): Science requirements, concept, and implementation. *Remote Sensing of Environment* 190:260-273. Mobley, C. D. , Light and Water: Radiative Transfer in Natural Waters, New York, NY, USA:Academic, Jan. 1994.

Morel, A., & Maritorena, S. (2001). Bio-optical properties of oceanic waters: A reappraisal. Journal of Geophysical Research: Oceans, 106(C4), 7163-7180

Morel, A. (1988). Optical modeling of the upper ocean in relation to its biogenous matter content (case I waters). Journal of geophysical research: oceans, 93(C9), 10749-10768

Neumann, T. A., A. Brenner, D. Hancock, J. Robbins, J. Saba, K. Harbeck, A. Gibbons, J. Lee, S. B. Luthcke, T. Rebold, et al. 2021. ATLAS/ICESat-2 L2A Global Geolocated Photon Data, Version 5. [Indicate subset used]. Boulder, Colorado USA. NASA National Snow and Ice Data Center Distributed Active Archive Center. https://nsidc.org/data/atl03/versions/6. [Accessed August 28, 2023].

Neuenschwander, A. L., & Magruder, L. A. (2019). Canopy and terrain height retrievals with ICESat-2: A first look. *Remote sensing*, *11*(14), 1721.

Parrish, C. E., Magruder, L. A., Neuenschwander, A. L., Forfinski-Sarkozi, N., Alonzo, M., & Jasinski, M. (2019). Validation of ICESat-2 ATLAS bathymetry and analysis of ATLAS's bathymetric mapping performance. *Remote sensing*, *11*(14), 1634.

Sayre, R., Noble, S., Hamann, S., Smith, R., Wright, D., Breyer, S., ... & Reed, A. (2019). A new 30 meter resolution global shoreline vector and associated global islands database for the development of standardized ecological coastal units. Journal of Operational Oceanography, 12(sup2), S47-S56.

Scheick, J., Arendt, A., Heagy, L., & Perez, F. (2019). Introducing icepyx, an open source Python library for obtaining and working with ICESat-2 data. Earth and Space Science Open Archive ESSOAr.

Scheick, J., Leong, W. J., Bisson, K., Arendt, A., Bhushan, S., Fair, Z., ... & Swinski, J. (2023). icepyx: querying, obtaining, analyzing, and manipulating ICESat-2 datasets. *Journal of Open Source Software*, *8*(84), 4912.

Siegel, D. A., Maritorena, S., Nelson, N. B., Behrenfeld, M. J., & McClain, C. R. (2005). Colored dissolved organic matter and its influence on the satellite-based characterization of the ocean biosphere. *Geophysical Research Letters*, 32(20).

Strand, K. O., Breivik, Ø., Pedersen, G., Vikebø, F. B., Sundby, S., & Christensen, K. H. (2020). Long-Term Statistics of Observed Bubble Depth Versus Modeled Wave Dissipation. *Journal of Geophysical Research: Oceans*, *125*(2), e2019JC015906.

Thomas, N., Pertiwi, A. P., Traganos, D., Lagomasino, D., Poursanidis, D., Moreno, S., & Fatoyinbo, L. (2021). Space-borne cloud-native satellite-derived bathymetry (SDB) models using ICESat-2 and Sentinel-2. *Geophysical Research Letters*, *48*(6), e2020GL092170.

Thomas, N., B. Lee, O. Coutts, P. Bunting, D. Lagomasino, and L. Fatoyinbo. 2022. A Purely Spaceborne Open Source Approach for Regional Bathymetry Mapping. *IEEE Transactions on Geoscience and Remote Sensing* 60:1-9.

Thorpe, S. (1992). Bubble clouds and the dynamics of the upper ocean. *Quarterly Journal of the Royal Meteorological Society*, 118(503), 1–22.

Yang, J., Zheng, H., Ma, Y., Zhao, P., Zhou, H., Li, S., & Wang, X. H. (2023). Examining the consistency of lidar attenuation coefficient K lidar from ICESat-2 and diffuse attenuation coefficient K d from MODIS. *IEEE Geoscience and Remote Sensing Letters*.

Wang, D., Wijesekera, H., Jarosz, E, Teague, W., & Pegau, W. (2016). Turbulent diffusivity under high winds from acoustic measurements of bubbles. *Journal of Physical Oceanography*, 46(5), 1593–1613.

Wang, C., Eidam, E., Pavelsky, T., Bisson, K., & Walker, C. (2023). An Open-Source Tool for Updating ICESat-2 ATL03 Land-Sea Masks with High-Resolution Shoreline Datasets (v1.1.0). Zenodo. https://doi.org/10.5281/zenodo.8432550

Zhang, X., Ma, Y., Li, Z., & Zhang, J. (2022). Satellite derived bathymetry based on ICESat-2 diffuse attenuation signal without prior information. *International Journal of Applied Earth Observation and Geoinformation*, 113, 102993.

Zheng, H., Ma, Y., Huang, J., Yang, J., Su, D., Yang, F., & Wang, X. H. (2022). Deriving vertical profiles of chlorophyll-a concentration in the upper layer of seawaters using ICESat-2 photon-counting lidar. *Optics Express*, 30(18), 33320-33336.